ROYAL SOCIETY
OF CHEMISTRY

PAPER

CrossMark
click for updates

Self-assembly of Pt-based truncated octahedral crystals into metal-frameworks towards enhanced electrocatalytic activity†

Yunpeng Zuo,‡[a] Tingting Li,‡[a] Huan Ren,[b] Guilin Zhu,[a] Kai Han,[a] Lin Zhuang[b] and Heyou Han*[a]

Self-assembly of Pt-based truncated octahedral crystals into frameworks has been demonstrated in this paper by suitably adjusting the reactant concentrations and temperature. This approach allows for control of Pt or Pt-based nano-crystals with subnanometer-size as building blocks for metal-frameworks (MFs): sub-micron porous tubes (SMPBs) and mesh (M). Both the Pt-based MFs exhibit enhanced activity and better stability for the oxygen reduction reaction (ORR) and methanol-oxidation reaction (MOR) than PtMFs. The mass activity (MA) of the Pt_4Cu-SMPBs (0.619 A mg^{-1}@0.9 V) exhibited 5.12 times enhancement over the commercial Pt/C (0.121 A mg^{-1}@0.9 V) catalyst towards the ORR and the value is well beyond the U.S. Department of Energy's 2017 target (0.44 A mg_{Pt}^{-1} @0.9 V). After 8000 cycles of accelerated durability test, the MA of the Pt_4Cu-SMPBs (0.411 A mg^{-1}@0.9 V) was still greater than the values of the Pt/C. These metal-framework materials provide a new direction to obtain highly open nanostructures which would readily improve their catalytic properties in both activity and durability while reducing their loading.

1. Introduction

Extensive research and development has been carried out to expand the application of fuel cells in automotives and portable electronic devices during the past few years.[1–10] The crucial factor for the development of fuel-cell technologies lies in the selection of appropriate catalysts which can effectively facilitate the cathode and anode reactions.[6–8] Among all the catalysts studied, platinum (Pt) is the most widely used catalyst for alcohols or hydrogen oxidation and oxygen reduction.[9–14] However, the extensive use of Pt catalysts is limited by the scarcity and high cost of Pt and low durability of the catalysts.[9–14] To date, the vast majority of the research studies have been performed on the development of Pt-based catalysts with excellent performance based on efficient utilization of materials with low cost.[10–12]

Specifically, the activity and durability can be enhanced by controlling the morphology of nanostructures in terms of the size, shape, and facets, thus exposing highly active atoms.[11,12] Among various methods for the synthesis of Pt-based

nanocrystals, solution-phase synthesis is identified as the most widely used route because of its capability to precisely control the properties of nanocrystals.[13–15] In addition to the traditional mechanism involved in solution-phase synthesis, the oriented attachment mechanism proposed by Penn and Banfield in 1998 shows a growth pathway which would reduce the total interfacial free energy of the system through the elimination of high energy facets to form three-dimensional (3D) structures using small particles as building blocks.[13,16] In particular, 3D structures can effectively improve the activity and stability of the catalyst, so it's necessary to find a suitable attachment method to achieve advanced nanoscale electrocatalysts with a high surface-to-volume ratio and 3D surface molecular accessibility.[16,17]

Another important factor, component, should also be considered at the same time,[17–25] because there still is a thorny problem that oxygenated intermediates might strongly bind to the bulk Pt surface for the oxygen reduction reaction (ORR).[6,25–27] So it's necessary to consider the generation of composite alloys with Pt-based facets having low surface oxygen affinity.[6,27]

What's more, it is also confirmed that the surface strain of PtM (M = Cu, Ni, *etc.*) nanocrystals (NCs) could alter the adsorption properties of the crystal surface to improve the catalytic activity of the catalyst.[7,28,29] Nevertheless, the synthesis of sub-nanometer level PtNCs still remains a great challenge, because NCs tend to agglomerate even when loaded on carbon.[12,13]

Using the solution method mentioned above, highly reactive Pt metal-frameworks (MFs) using sub-nanometer PtNCs as

[a]*State Key Laboratory of Agricultural Microbiology, College of Science, Huazhong Agricultural University, Wuhan 430070, P. R. China. E-mail: hyhan@mail.hzau.edu.cn*
[b]*College of Chemistry and Molecular Sciences, Hubei Key Lab of Electrochemical Power Sources, Wuhan University, Wuhan 430072, P. R. China*

‡ These authors contributed equally to this work.

This journal is © The Royal Society of Chemistry 2016

J. Mater. Chem. A, 2016, 4, 15169–15180 | 15169

building blocks can effectively enhance the structural stability of the catalysts.

In this paper, we developed an attachment-based growth method which uses Pt and Pt_4Cu truncated octahedral crystals with a uniform size (~5 nm) as building blocks to form MFs such as Pt or Pt_4Cu mesh (M) and sub-micron porous tubes (SMPBs). The synthetic process was performed under reflux conditions using N,N-dimethylformamide (DMF) as the solvent and reducing agent, and oleic acid as the morphology-directing agent at 180 °C for 30 min to obtain Pt and Pt_4Cu truncated octahedral crystals, followed by heating at around 230 °C for about 40 min to obtain Pt or Pt_4Cu-M or -SMPBs (the experimental details are provided in the Experimental section). The as-prepared Pt_4Cu-SMPBs and Pt_4Cu-M were found to exhibit higher specific and mass activities than commercial Pt/C in both the ORR and the methanol oxidation reaction (MOR).

2. Experimental section

Preparation

Synthesis of Pt_4Cu-SMPBs. In a typical synthesis, 540 μL H_2PtCl_6 (~19.3 mM), 50 μL $Cu(NO_3)_2$ (~48 mM) and 5 mL oleic acid were dispersed in 8 mL of DMF, and then the mixture was under ultrasonication for 30 min. The reactants were added into a reaction bottle at 180 °C under constant magnetic stirring. With the reaction proceeding, the color of the solution gradually changed, and after 25 min the system was heated up to 230 °C for an additional 30 min. The final products obtained by centrifugation were dispersed in 15 mL of ethanol. The solution was heated at 60 °C for 4 h to clean the surface of the particles, and then they were washed with hexitol three times.

Synthesis of Pt_4Cu-M. In a standard procedure, 540 μL H_2PtCl_6 (~19.3 mM), 50 μL $Cu(NO_3)_2$ (~48 mM) and 5 mL oleic acid were dispersed in 16 mL of DMF, and then the products were processed according to the above method just as the synthesis of Pt_4Cu-SMPBs.

Characterization

Transmission electron microscopy (TEM) images and high-resolution transmission electron microscopy (HRTEM) and high-angle annular dark field-scanning transmission electron microscopy (HAADF-STEM) measurements were taken using a FEI-Tecnai G2 F30 transmission electron microscope at an accelerating voltage of 200 kV. The energy-dispersive X-ray spectroscopy (EDS) analysis was also done using a field emission scanning electron microscope (FESEM) with an EDAX attachment operating at an accelerating voltage of 30 kV. The FESEM measurements were taken using a SU8010. The compositions of Pt nanomaterials were determined by inductively coupled plasma mass spectrometry (ICP-MS) (NexION 300Q, PerkinElmer). The X-ray diffraction (XRD) analysis was carried out on a Bruker D8 Advance X-ray diffractometer with Cu K_α radiation. The X-ray photoelectron spectra (XPS) analysis was performed by using an ESCALAB 250Xi and calibrated by using the C 1s peak (284.6 eV).
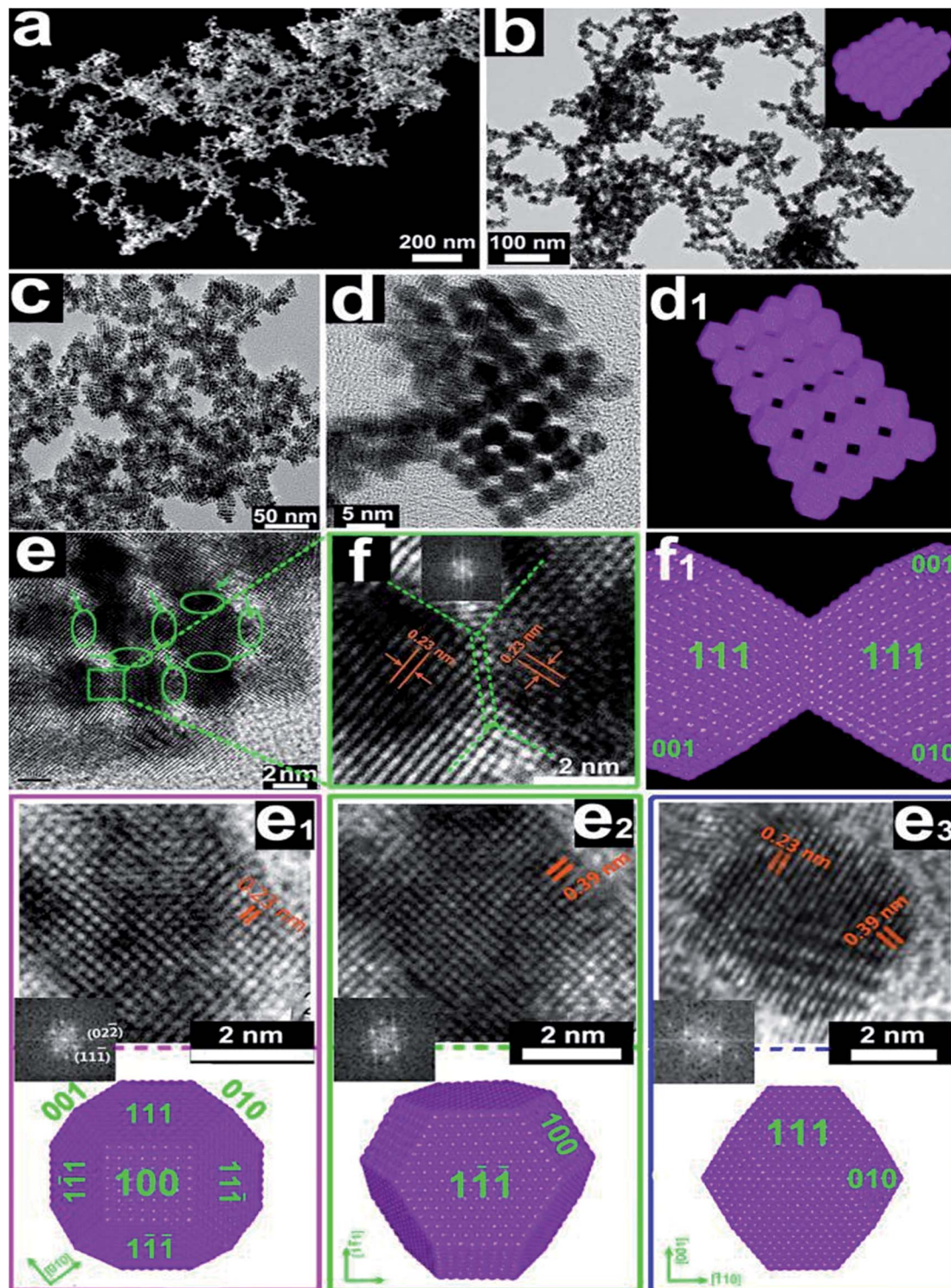
Electrochemical measurements

To compare the ORR activities of the Pt-SMPB/-M, Pt_4Cu-SMPB/-M, and commercial Pt/C, the catalysts were re-dispersed in a mixture of 0.5 mL DI water and 0.5 mL isopropanol under ultrasonication for 20 min. Then 20 μL of 5% Nafion was added under ultrasonication for 30 min to obtain Pt ink. Then the concentrations of Pt and Cu were determined by ICP-MS. Finally, the Pt ink was deposited on a pre-cleaned GC-RDE (Pine Research Instrumentation) with an area of 0.196 cm^2 and the loading amounts of Pt are nearly 25 μg cm^{-2}. Cyclic voltammetry (CV) tests were performed at room temperature in N_2-purged 0.1 M $HClO_4$ solution with a sweep rate of 50 mV s^{-1}. The ORR activity was measured in the potential range of 0.05–1.2 (V vs. RHE) in O_2-saturated 0.1 M $HClO_4$ solution with a sweep rate of 10 mV s^{-1} and a rotation rate of 1600 rpm. The catalytic durability of the Pt_4Cu-SMPB/-M catalysts was evaluated through accelerated tests by applying linear potential sweeps in the range between 0.6 and 1.0 V for a duration of 8000 potential cycles at a sweep rate of 0.1 mV s^{-1} in an O_2-saturated 0.1 M $HClO_4$ solution.

3. Results and discussion

The macro performance of the catalyst reflects the living characteristics of the structure.[30–37] Similarly, Pt-M was prepared by a rolling process by controlling the ratio of the reactants, and the Pt truncated octahedral particles were assembled in a special manner to generate 3D structures that offer substrate molecular accessibility.[16] Fig. 1 shows the 3D mesh structure, and Fig. 1a–e exhibit the HAADF-STEM and enlarged HRTEM images of Pt-M nanostructures. This unique structure is like a building with blocks, with the separate nano-crystals self-assembling to tensegrity as indicated by the enlarged HRTEM images in Fig. 1c–e. The HRTEM image of the adjacent connected Pt truncated octahedral particles (Fig. 1f) and the corresponding structure modeling (Fig. $1f_1$) clearly show the regular array of Pt atoms, which reveals that each Pt truncated octahedral particle can connect the adjacent NCs by the terminal atoms closely attached without defects. This conclusion could be further verified by the Fast Fourier Transformation (FFT) pattern insets in Fig. $1f_1$, which show the integrity of the connecting structure. Three typical principal projections of the initial Pt particles in Fig. $1(e_{1,2,3})$ show a morphology of truncated octahedral particles through the comparison of the ideal structure model as shown at the bottom. The results clearly show the morphological integrity of the Pt particles. The identical FFT patterns shown in the insets revealed the integral crystal structure of Pt truncated octahedral particles with single crystallinity.[38,39]

By adjusting the parameters of the reaction system, different attachment mode structures can be obtained. The TEM image of Pt-SMPBs and the illustrations in Fig. 2a show the MF structure for the attachment mode of Pt-SMPBs. This constructed structure based on Pt truncated octahedral NCs contains lots of pore architectures which can be well verified separately by the HRTEM and HAADF-STEM images of Pt-

15170 | J. Mater. Chem. A, 2016, **4**, 15169–15180

This journal is © The Royal Society of Chemistry 2016

Fig. 1 (a) HAADF-STEM images of Pt-M nanostructures, (b–e) enlarged HRTEM images of Pt-M show that each Pt truncated octahedral particle can connect the adjacent NCs by the terminal atoms closely attached without defects. (f) HRTEM image of the adjacent connected Pt truncated octahedral particles and (f_1) the corresponding structure modeling. ($e_{1,2,3}$) Three typical principal projections of the initial Pt particles show the morphology of truncated octahedral particles through the comparison of the ideal structure model as shown at the bottom. The identical FFT patterns shown in the insets revealed the integral crystal structure of Pt truncated octahedral particles with single crystallinity.

SMPBs in Fig. 2b–d. Pt truncated octahedral NCs might be arranged in an intensive and orderly stacked manner, together with micro-staggered mesh growth as a firm porous framework structure (Fig. 2c and $c_{1,2,3}$). The FESEM image in Fig. S1† shows the distribution of Pt-SMPBs with a well-distinguished morphology. The attachment of the adjacent NCs involves both
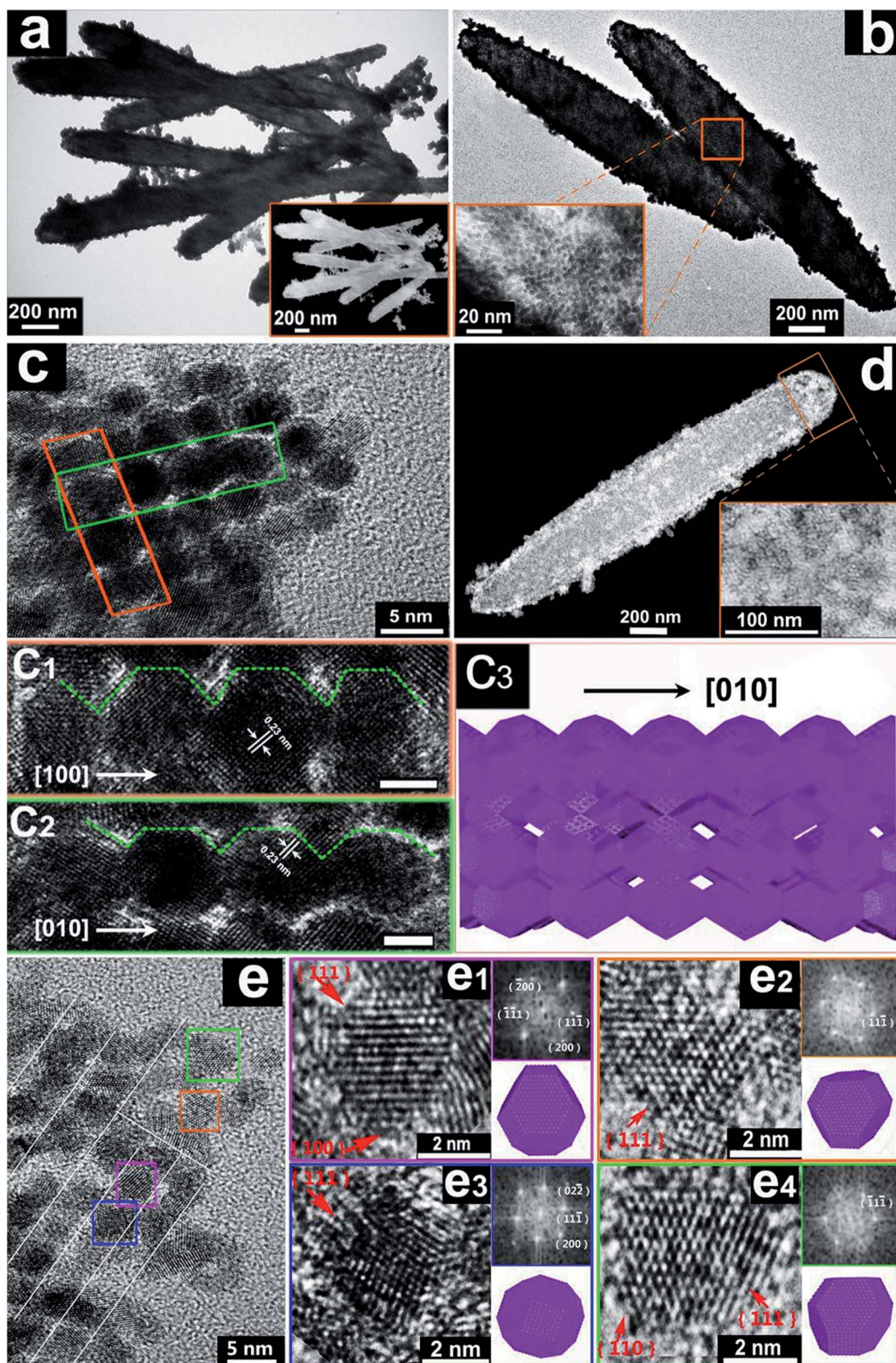
Fig. 2   Structural analyses of the Pt-SMPBs. (a) The TEM and the illustrations show the metal-framework structure for the attachment mode of Pt-SMPBs, and the inset shows Pt truncated octahedral NCs as building blocks for the structure, (b) the HRTEM image of Pt-SMPBs is similar to the HAADF-STEM image (d), and the HRTEM images in c and $c_{1,2}$ exhibit the attachment mode for the SMPB structure. (c_3) The corresponding geometrical model to c and $c_{1,2}$. (e) HRTEM image of the selected area of Pt-SMPBs with a uniform size for crystal alignment; ($e_{1,2,3,4}$) HRTEM images of single NCs taken from four typical principal projections of the initial Pt truncated octahedral consistent with the ideal structure model as shown at the bottom-right, with the corresponding color outline of the rectangular box in (e), top-right insets in $e_{1,2,3,4}$ show the corresponding FFT pattern of the selected NCs revealing Pt truncated octahedral particles with single crystallinity. The scale bar in $C_{1,2}$ is 2 nm.
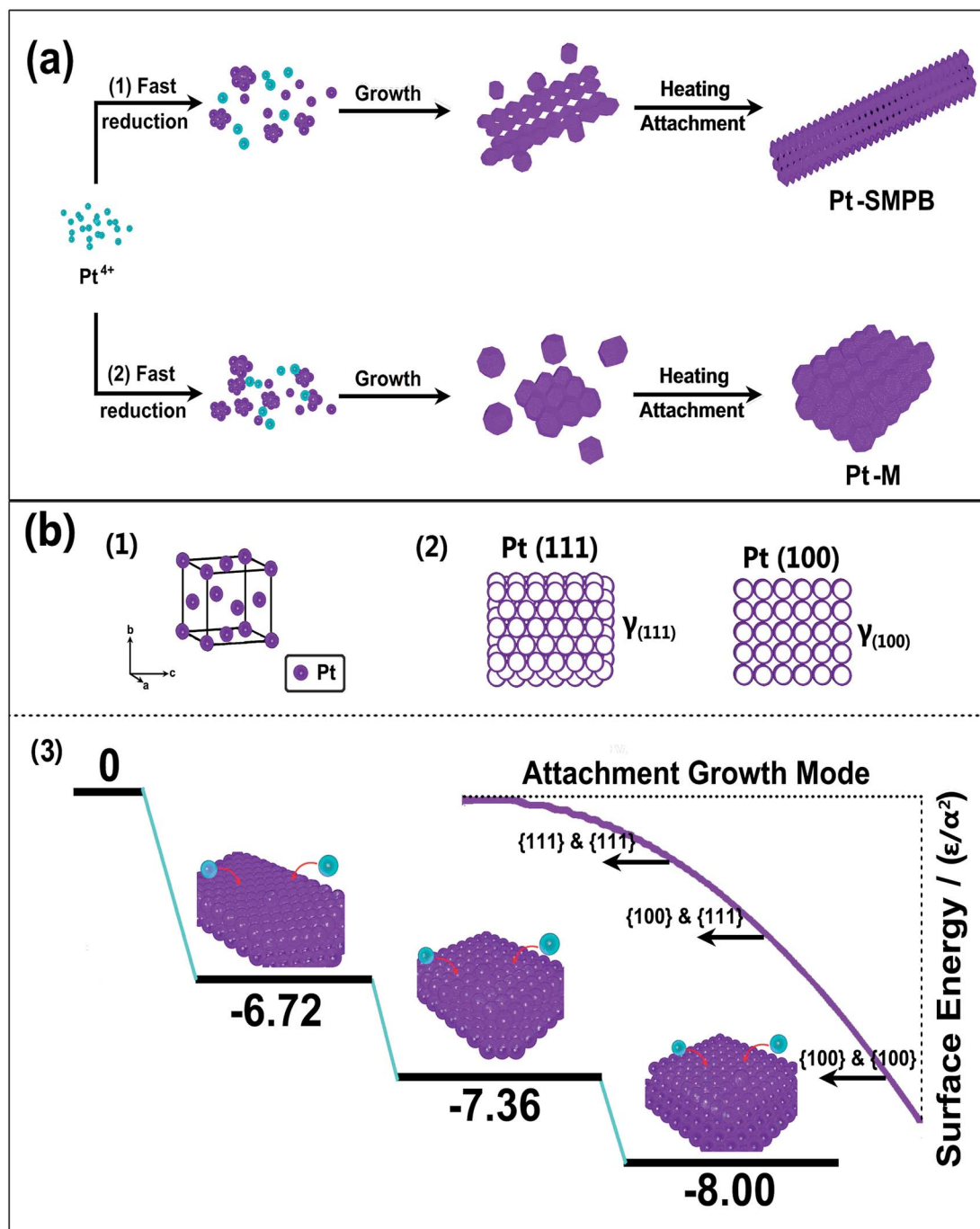
Fig. 3 Schematic illustration of the fabrication process for the Pt-SMPB/-M catalyst. (a) A schematic illustration of the nucleation, growth, attachment, and final morphology of Pt nanostructures in the synthesis. (b_1) Unit cell of the fcc lattice shared by Pt. (b_2) Simulation diagrams of the arrangement of {111} and {100} facets of Pt atoms. (b_3) The curve of surface energy *versus* three attachment growth modes.

lateral growth and longitudinal growth modes as shown in Fig. 2c and $c_{1,2,3}$. The attachment mode along [100] or [010] can effectively reduce the interfacial energy of the system. Fig. 2c and e show the HRTEM images of the selected area of Pt-SMPBs with a uniform size (~5 nm) for crystal alignment, and the diameter of the Pt truncated octahedral particles was measured by HRTEM. TEM images of single NCs in Fig. $2e_{1,2,3,4}$ were taken from four typical principal projections of the initial Pt truncated octahedral particles consistent with the ideal structure model as shown in bottom-right, with the corresponding color outline of the rectangular box in Fig. 2e; top-right insets in ($e_{1,2,3,4}$) show that the corresponding FFT pattern of the selected NCs revealed Pt truncated octahedral particles with single crystallinity.[38,39] FESEM and HAADF-STEM images in Fig. S1† are the supplement to the above conclusion, which clearly show the sub-micron porous tubes. It is worth noting that TEM images in
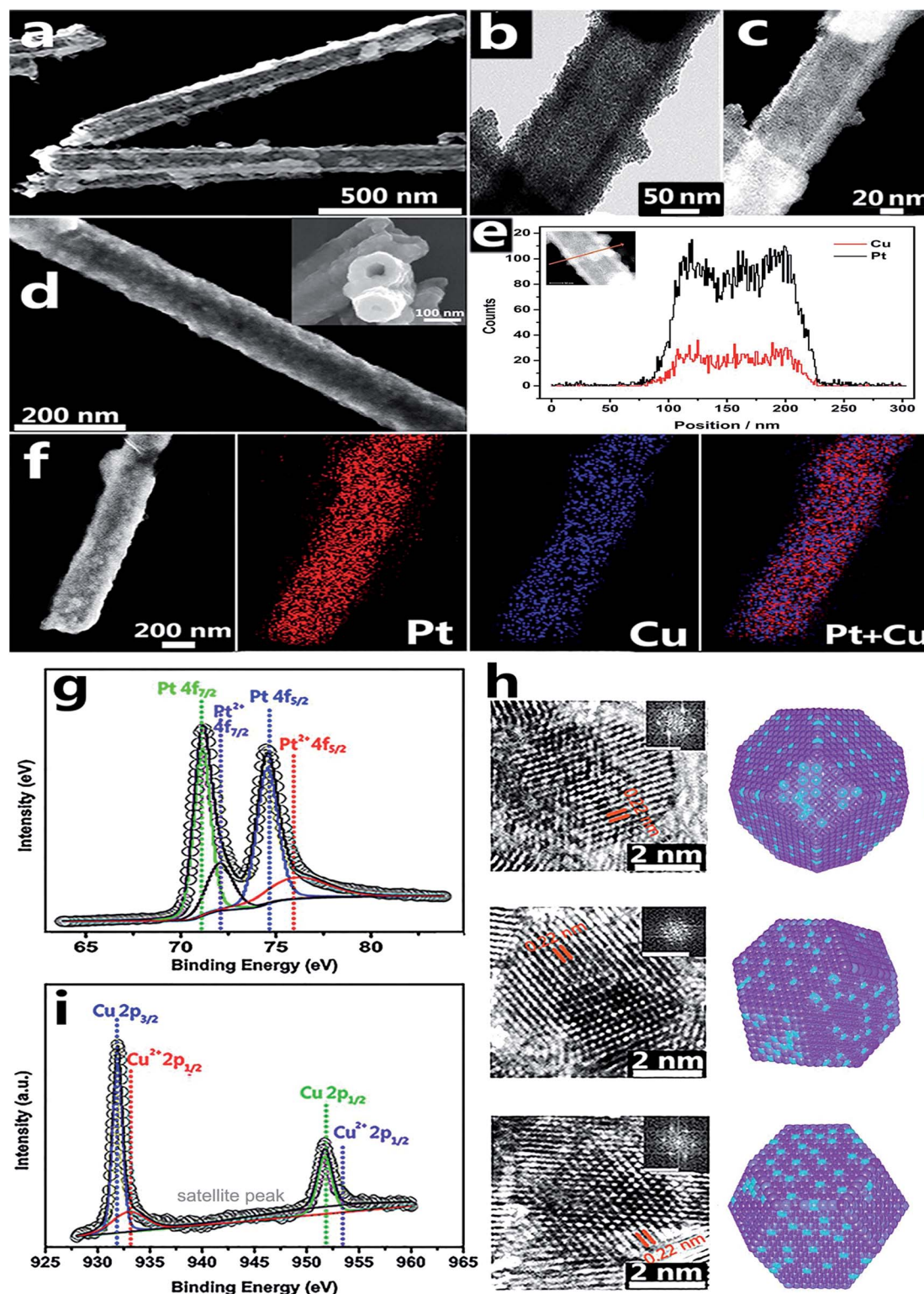
Fig. 4 Structural and compositional analyses of the Pt$_4$Cu-SMPB catalysts. (a) HAADF-STEM image of Pt$_4$Cu-SMPBs. (b and c) The HRTEM and STEM images of Pt$_4$Cu-SMPBs show Pt$_4$Cu truncated octahedral NCs as building blocks for the SMPBs. (d) FESEM images of Pt$_4$Cu-SMPBs and the inset clearly show the tubular structure. (e and f) TEM-EDX line-scanning profile across an individual porous tube and FESEM-EDX elemental mapping shows the distribution of Pt/Cu in different parts. (g and i) Pt 4f and Cu 2p XPS spectra of the Pt$_4$Cu-SMPB catalyst. (h) Three typical principal projections of the Pt$_4$Cu particles reveal the morphology of truncated octahedral particles with single crystallinity.
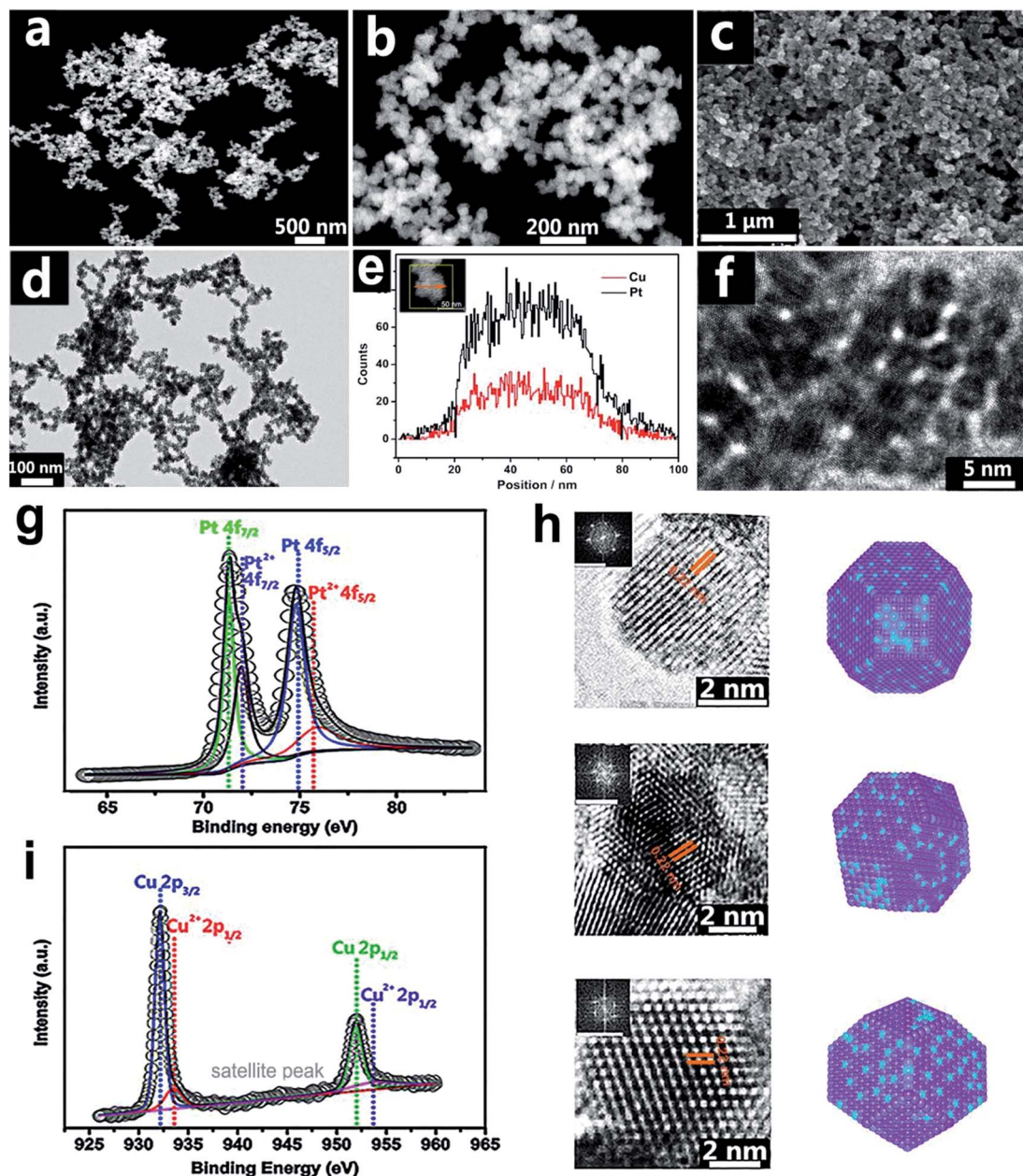
Fig. 5 Structural and compositional analyses of the Pt₄Cu-M catalysts. (a–c) Enlarged HAADF-STEM and FESEM images of Pt₄Cu-M. (d and f) HRTEM images of the selected area of Pt₄Cu-M with a uniform size for crystal alignment. (e) TEM-EDX line-scanning profile across an individual mesh structure. (g and i) Pt 4f and Cu 2p XPS spectra of the Pt₄Cu-M catalyst. (h) Three typical principal projections of the Pt₄Cu particles reveal the morphology of truncated octahedral particles with single crystallinity.

Fig. S2† show the samples taken during the reaction. The Pt truncated octahedral NCs assemble into a two-dimensional grid (Fig. S2a and b†), and then curl into the SMPBs under the synergism of {111} & {100} and {100} & {100} attachment modes because of the mutative temperature process.

It has been proved that the formation of metal nanocrystals consists of nucleation and growth steps, and the precursor or capping agent-determined reaction kinetics can affect the nucleation, growth and attachment progress.[1,4] When chloroplatinic acid (blue spheres in Fig. 3a) used as the Pt precursor is mixed with reactants, a large number of zero-valent Pt atoms

(violet spheres in Fig. 3a) could be generated in the initial event. The homogeneous nucleation would start when the content of Pt atoms reached the level of supersaturation.[4,40] The Pt atoms agglomerate to form small clusters and the small Pt particles would aggregate into truncated octahedral crystals after the introduction of oleic acid in this system. Meanwhile, Fig. 3a shows that the attachment mode would vary due to the different concentrations of oleic acid and Pt crystals for the two reaction conditions. It was worth noting that the structural stability for a given volume of nanocrystals is inversely proportional to the γ based on the Woolf theory.[4,40–43] The Pt nuclei would grow into

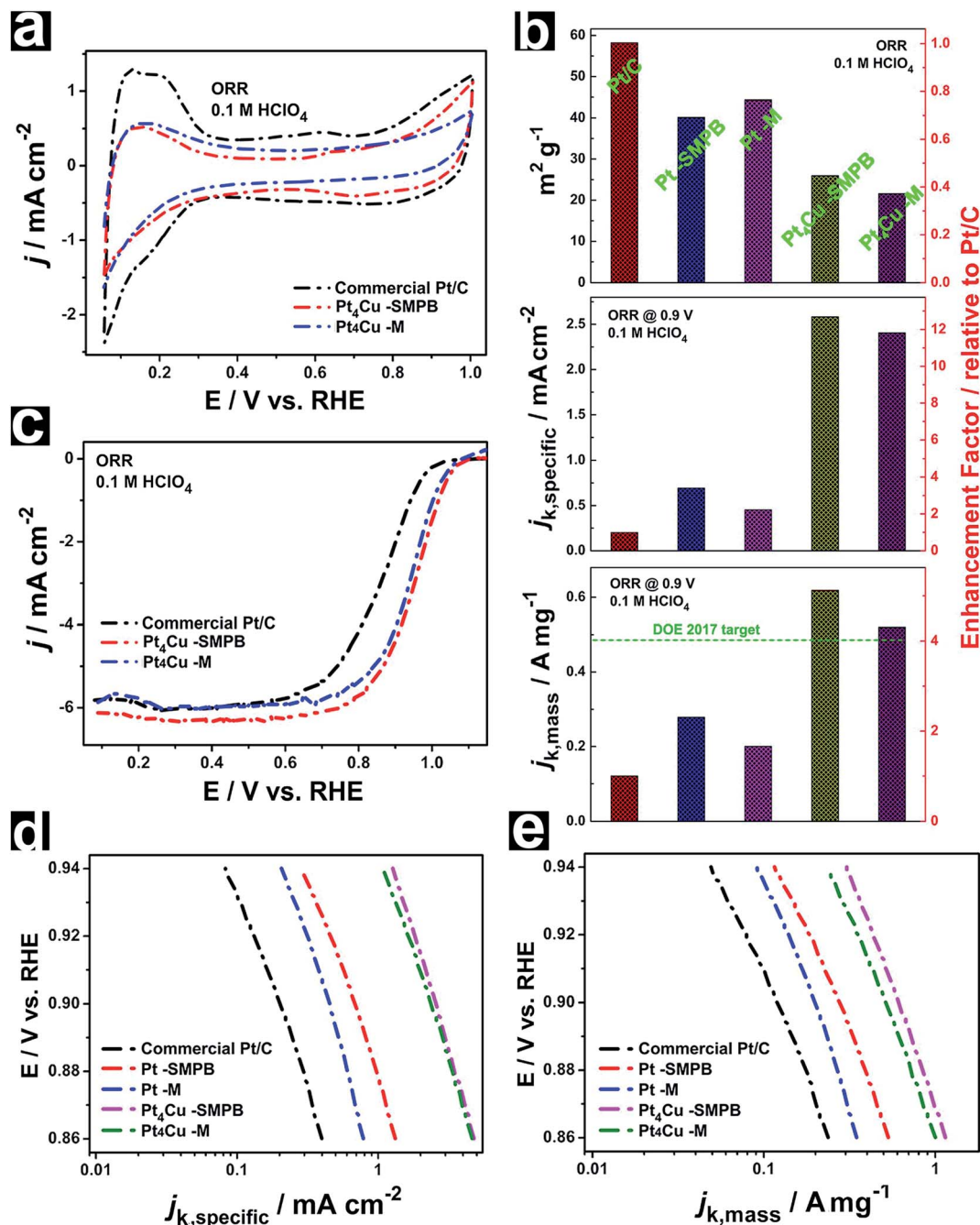**Fig. 6** (a) CVs of Pt/C and Pt$_4$Cu-SMPB/-M were recorded at room temperature in N$_2$-purged 0.1 M HClO$_4$ solution at a sweep rate of 50 mV s^{-1}. (b) The ECSA (top), specific activity (middle), and mass activity (bottom) at 0.9 V *versus* RHE for Pt/C and Pt-SMPB/-M, and Pt$_4$Cu-SMPB/-M catalysts, which are given as kinetic current densities (j_k) normalized to the ECSA and Pt masses of the catalysts, respectively. (c) ORR polarization curves of the above catalysts. In (a) and (c), the currents were normalized to the geometric area of the RDE (0.196 cm^2). (d and e) Tafel plots (potential *versus* kinetic current density) of Pt/Pt$_4$Cu-SMPB/-M and Pt/C.

relatively small Pt particles which tend to attach to each other due to the relatively high surface energy and low surface charge, thus minimizing the total interfacial free energy (γ) of the system.[4,40,41] Meanwhile, the XRD pattern of Pt-SMPB/-M in Fig. S3† shows that the typical peaks are consistent with face-centered cubic (fcc) Pt with a lattice constant of $a = 0.39$ nm, which can be indexed to the standard literature values (JCPDS no. 04-0802).[44] For the Pt (fcc), the γ of the low-Miller index

crystallographic facets can be estimated as follows: $\gamma\{111\} = 3.36(\varepsilon/\alpha^2)$, and $\gamma\{100\} = 4(\varepsilon/\alpha^2)$.[4,42,43] The truncated octahedral particles were covered alternately by four $\{111\}$ facets and four $\{100\}$ facets, and there were three attachment modes for the terminal atoms: $\{111\}$ & $\{100\}$, $\{111\}$ & $\{111\}$, and $\{100\}$ & $\{100\}$. The most appropriate connection sequence implies that the whole block material should minimize the total surface energy. A unit cell of the fcc lattice shared by Pt and the simulation

15176 | *J. Mater. Chem. A*, 2016, **4**, 15169–15180

This journal is © The Royal Society of Chemistry 2016

diagrams of the arrangement of {111} and {100} facets are shown in Fig. 3b$_{1,2}$. Despite three different growth modes of the terminal atoms, the crystal surface of each particle in the same family of crystal planes can be combined with four particles in its surroundings with an equal probability. Thus, two particles can be used as a model to simulate the formation process of the mesh structure. The surface energy would reduce 2γ{111} when the binding mode is {111} & {111}, while it would reduce (γ{111} + γ{100}) and 2γ{100} in accordance with the binding modes {111} & {100} and {100} & {100}, respectively. Collectively, when the binding mode is {100} & {100}, the γ of the bulk materials is the minimum as shown in Fig. 3b$_3$. So the {100} & {100} growth mode without defects would be the main bridge in the construction of the 3D mesh stereo structure. To support the universality of the conclusion, the curve of surface energy *versus* growth mode has been made and shown in Fig. 3b$_3$. The HRTEM images in Fig. 1, 2 and S2† could further confirm the aforementioned conclusion.

PtCu-based nanocatalysts have been shown to be one of the most efficient compositions for the ORR.[44–47] On the basis of the aforementioned synthesis system, Pt$_4$Cu truncated octahedral particles as well as the Pt$_4$Cu-SMPBs and Pt$_4$Cu-M were obtained. For Pt$_4$Cu, the HRTEM images (Fig. 4h and 5h) and the typical peaks in XRD patterns (Fig. S4†) of the bimetallic

products could be indexed to those of fcc Pt$_4$Cu.[44,47] The Pt/Cu composition of 4/1 was confirmed by means of both ICP-MS and transmission electron microscopy with an energy dispersive X-ray (TEM-EDX). The overall molar ratios of Pt and Cu in Pt$_4$Cu-SMPBs and Pt$_4$Cu-M obtained from ICP-MS were 80.23 : 19.77 and 80.87 : 19.13, respectively. The details are shown in Table S1.† Fig. 4a shows the HAADF-STEM image of Pt$_4$Cu-SMPBs with the intense contrast for the 3D porous structure which is conducive to promoting the molecular accessibility. The STEM and HRTEM images in Fig. 4b and c clearly illustrate Pt$_4$Cu truncated octahedral particles as the building blocks for the micrometer porous tube. FESEM images (Fig. 4d and the inset image) can further present the tight and 3D porous-tubular structures of Pt$_4$Cu-SMPBs. The enlarged STEM images in Fig. 5a and b show the 3D mesh morphology. The attachment form of two adjacent particles in the Pt$_4$Cu-M is similar to that of Pt-M when compared the HRTEM images shown in Fig. 1e and 5f. The attachment form through the binding of terminal atoms can effectively provide rigid 3D reticular structures to ensure the highly active performance of the catalysts.[16] Meanwhile, as shown in Fig. 5c and d, large amounts of Pt$_4$Cu-M accumulate within the layers, which is consistent with the fact that the attachment manner between Pt$_4$Cu-M truncated octahedron particles can still maintain a relatively independent
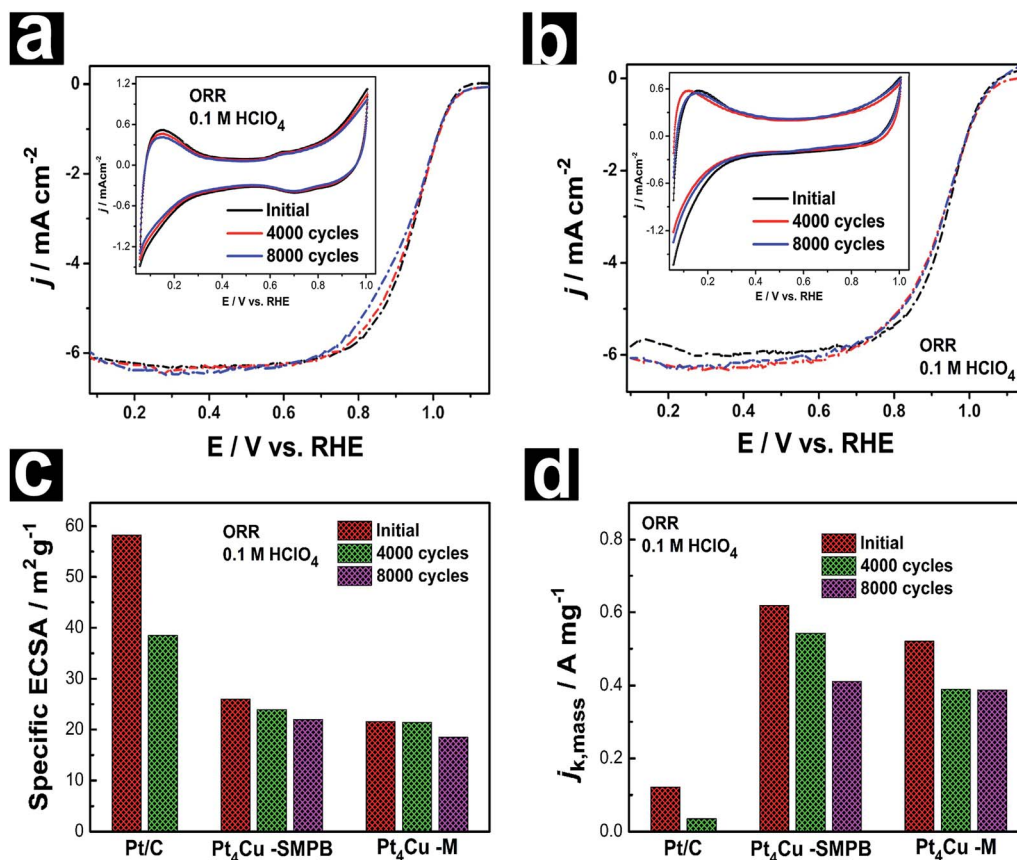

Fig. 7 Electrochemical durability of Pt$_4$Cu–SMPBs and -M. (a and b) ORR polarization curves of Pt$_4$Cu–SMPB/-M recorded before and after 4000/8000 potential cycles respectively, and (insets) corresponding CVs between 0.05 and 1.2 V *versus* RHE. (c) The specific ECSA and (d) the mass activities at 0.9 V *versus* RHE of the catalysts before and after acceleration tests.

space structure resulting from kinetics-induced self-assembly. EDX elemental mapping results of Pt$_4$Cu-SMPBs (Fig. 4f) suggest that all elements are homogeneously distributed whereas the TEM-EDX line-scanning profile across individual porous tubes (Fig. 4e) shows the distribution of Pt/Cu in different parts. The oxidation state of bimetallic nanostructures of Pt$_4$Cu-M and Pt$_4$Cu-SMPBs was measured by XPS. The Cu 2p and Pt 4f XPS spectra of Pt$_4$Cu-SMPBs and Pt$_4$Cu-M (Fig. 4g and i and 5g and i) obtained in a vacuum show that the majority of the surface Cu and Pt were mainly in the metallic state.[47] The surface information about Pt$_4$Cu-M showed that the Pt $4f_{7/2}$ and $4f_{5/2}$ had a binding energy of 71.33 eV and 74.80 eV, respectively, a little higher than the corresponding values of Pt$_4$Cu-SMPBs. The Cu $2p_{3/2}$ and $2p_{1/2}$ of Pt$_4$Cu-M had a binding energy of 932.19 eV and 951.97 eV, which is identical to the trend of Pt$_4$Cu-SMPBs. The results might be ascribed to the special binding modes ({111} & {100} and {100} & {100}) of the Pt$_4$Cu-SMPBs which further verified the mechanism proposed above.[44–47] The XRD pattern shown in Fig. S4† indicated that the as-obtained Pt$_4$Cu-SMPBs and Pt$_4$Cu-M were composed of the elements Pt and Cu, because all the diffraction peaks could be indexed to the fcc Pt (JCPDS no. 05–2868) and Cu (JCPDS no. 05–0836).[44] The broadening of the peaks can be attributed to the relatively small size of the nanoparticles.[47] HRTEM images taken from individual particles from three typical principal projections showed a single-crystal structure with well-defined fringes (Fig. 4h and 5h), and the marked lattice fringes corresponded to the d spacing of the (111) facet of the Pt$_4$Cu alloy.

It is well-established that the specific activity of Pt towards the ORR can be dramatically enhanced by introducing other metal atoms, which might be attributed to the weakening of the binding properties of adsorbates (O and OH).[28,48] Inspired by this, the electrocatalytic properties of the Pt$_4$Cu-SMPBs and Pt$_4$Cu-M were evaluated in comparison with commercial Pt/C (20% Pt). The CV curves of these catalysts in Fig. 6a and S5a† were recorded at room temperature in N$_2$-purged 0.1 M HClO$_4$ solutions at a sweep rate of 50 mV s^{-1}. The CVs reveal the difference in surface coverage by H$_{upd}$ and OH$_{ad}$.[16] We

calculated the electrochemically active surface area (ECSA) by measuring the charge collected in the H$_{upd}$ adsorption/desorption region (H$^+$ + e$^-$ = H$_{upd}$, 0.05 V < E < 0.38 V) after double-layer correction and assuming a value of 210 μC cm^{-2} for the adsorption of a hydrogen monolayer.[48] Owing to the high dispersion of Pt atoms, the ECSA per g$_{Pt}$ of the commercial Pt/C (58.24 m^2 g^{-1}) was much higher than that of the Pt-SMPBs (40.19 m^2 g^{-1})/-M (44.38 m^2 g^{-1}) and Pt$_4$Cu-SMPBs (25.99 m^2 g^{-1})/-M (21.63 m^2 g^{-1}). Therefore, catalysts were loaded onto a glassy carbon electrode with a surface area of ∼0.196 cm^2 and at a Pt loading amount of nearly 25 μg cm^{-2}.

Fig. 6c and S5b† show the ORR polarization curves of the catalysts. The diffusion-limiting currents were obtained in the potential region below 0.6 V, whereas a mixed kinetic-diffusion control region occurs above 0.6 V. The Koutecky–Levich (K–L) equation was used to analyze the kinetic currents of the ORR polarization curves and the ORR performance in the diffusion and kinetically limited regions normalized against the glassy carbon area (0.196 cm^2), the ECSA and Pt mass, to obtain the specific and mass activities ($j_{k,specific}$ and $j_{k,mass}$), respectively.[48–50] Relative to the commercial Pt/C, the Pt-SMPB/-M and Pt$_4$Cu-SMPB/-M catalysts showed enhanced activity with respect to the $j_{k,specific}$ and $j_{k,mass}$ values in the potential region between 0.8 and 0.96 V, especially Pt$_4$Cu-SMPB/-M. As shown in Fig. 6b, the Pt$_4$Cu-SMPB/-M catalysts had the $j_{k,specific}$ values of 2.58 mA cm^{-2} and 2.41 mA cm^{-2}, and $j_{k,mass}$ values of 0.619 A mg^{-1} and 0.521 A mg^{-1} at 0.9 V, whereas the corresponding values were 0.204 mA cm^{-2} and 0.121 A mg^{-1} for the Pt/C catalyst, 0.694 mA cm^{-2} and 0.279 A mg^{-1} for Pt-SMPB, and 0.454 mA cm^{-2} and 0.201 A mg^{-1} for Pt-M. Both the $j_{k,specific}$ and $j_{k,mass}$ values of the Pt$_4$Cu-SMPB/-M at 0.9 V are greatly enhanced compared with the Pt/C and Pt-SMPB/-M catalysts and those of the state of the art PtCu catalysts recently reported (Table S2†). It can be seen that Pt$_4$Cu-SMPB and Pt$_4$Cu-M demonstrated significantly enhanced electrocatalytic activity and stability compared with the relevant materials published in recent studies. At 0.9 V, the $j_{k,mass}$ values of the Pt$_4$Cu-SMPB/-M catalysts were higher than the U.S. Department of Energy's 2017
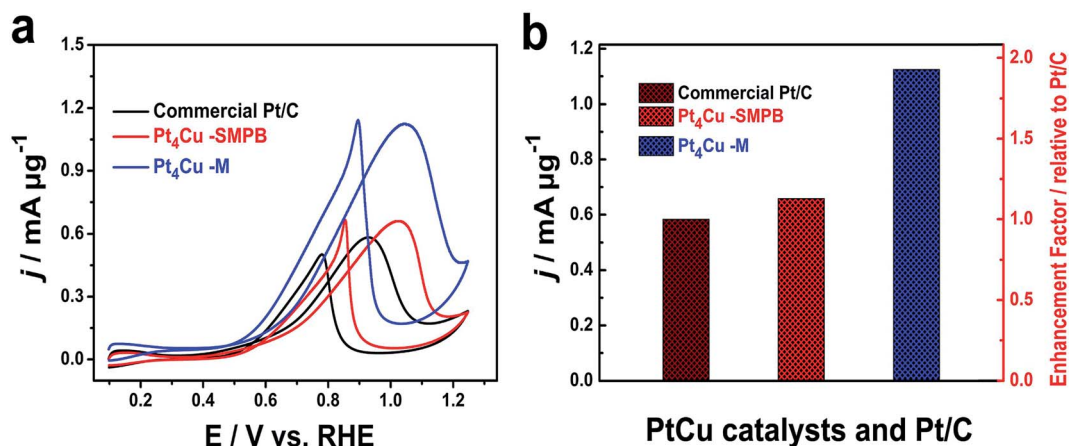

Fig. 8 Pt$_4$Cu-SMPB and -M as high-performance electrocatalysts towards the MOR. (a) CV curves of the MOR in 0.1 M HClO$_4$ + 0.2 M CH$_3$OH solution at a scan rate of 50 mV s^{-1}. (b) Mass activities for the MOR given as j normalized to the loading amount of Pt of the catalysts.

target (0.44 A mg_{Pt}^{-1}),[16,27] and the $j_{k,mass}$ of the Pt$_4$Cu-SMPBs is larger than that of the Pt$_4$Cu-M, mainly due to the larger contact area with the substrate molecules.[16] Moreover, the values of $j_{k,specific}$ and $j_{k,mass}$ also reveal that Cu can dramatically enhance the activity of Pt-based nanomaterials towards the ORR.[44,47] It is worth noting that the corresponding Tafel plots (potential *versus* kinetic current density) of Pt$_4$Cu-SMPB/-M and Pt/C plotted in Fig. 6d and e indicate that Pt$_4$Cu-SMPB/-M is superior to Pt/C toward the ORR.

In addition to the greatly enhanced specific and mass activities, both the Pt$_4$Cu-SMPBs and Pt$_4$Cu-M exhibited significant catalytic durability and intrinsic stability. The catalytic durabilities of the Pt$_4$Cu-SMPB/-M samples were evaluated through acceleration tests by applying linear potential sweeps in the range between 0.6 and 1.0 V *versus* RHE for a duration of 8000 potential cycles at a sweep rate of 0.1 mV s^{-1} in an O$_2$-saturated 0.1 M HClO$_4$ solution (Fig. 7a and b). The catalytic durabilities of the Pt$_4$Cu-SMPBs and Pt$_4$Cu-M were greatly improved relative to the Pt/C in terms of both the specific surface area and $j_{k,mass}$ at 0.9 V. For the Pt/C, 4000 cycles caused a substantial loss of the specific ECSA ($\sim$33.88%, Fig. 7c) because of dissolution of surface Pt atoms and agglomeration of Pt particles through the surface redox process. However, for the Pt$_4$Cu-SMPB/-M, the losses of the specific ECSA after 4000 potential cycles were $\sim$7.8% and $\sim$0.9%, respectively. Moreover, the catalytic stability of Pt$_4$Cu-SMPB/-M obtained here is superior or comparable to the relevant materials previously reported by others (Table S2†). Fig. S6a and S6b† show the CVs and ORR polarization curves of commercial Pt/C before and after an accelerated durability test (ADT), respectively. As shown in Fig. S6b,† both the half wave potential and the limit current are drastically reduced, and Pt-SMPBs and Pt-M showed a similar tendency (Fig. S7† and 8). Moreover, the Pt/C showed a substantial loss of $j_{k,mass}$ ($\sim$71%, 0.0351 A mg^{-1}) and $j_{k,specific}$ ($\sim$56.2%, 0.0893 A cm^{-2}). After 4000 and 8000 potential cycles, the Pt$_4$Cu-SMPB/-M catalysts largely retained the ECSA and mass activity (Fig. 7c and d), with only $\sim$1 and $\sim$5 mV shifts for the half wave potential, respectively. After 8000 cycles, the mass activities of the Pt$_4$Cu-SMPB/-M catalysts were still as high as 0.411 A mg^{-1} and 0.387 A mg^{-1}, respectively. As shown in Fig. S9a and b,† the mass activities of the ORR were given as $j_{k,mass}$ normalized to the Pt masses of the Pt$_4$Cu-SMPB/-M before and after 4000 and 8000 cycles for the catalytic durability of the catalysts. Additionally, STEM and TEM images in Fig. S10† confirmed that the SMPB and M structures were preserved before and after cycles. However, we found that the structure of sub-micron porous tubes was divided into several short porous tubes as shown in Fig. S10a and b,† which might be caused by the strong ultrasonic cleaning of the catalysts from the electrode. Fig. S10c–f† show the structure of PtCu nanoparticles and Pt/C before and after the ADT test. The morphology of the PtCu particles showed almost no change while the sub-nanometer Pt nanoparticles in the commercial Pt/C aggregated to form big particles after the ADT test, as the limit current density was negligible after 8000 potential cycles (Fig. 7a) and the basic composition unit remained almost unchanged.

These Pt$_4$Cu-SMPB/-M catalysts were also applied as electrocatalysts for the MOR and compared with Pt/C in 0.1 M HClO$_4$ + 0.2 M CH$_3$OH solution at a scan rate of 50 mV s^{-1} as shown in Fig. 8. Particularly, the Pt$_4$Cu-SMPBs and -M catalysts exhibited notably higher electrocatalytic activity than commercial Pt/C toward the MOR (Fig. 8a). To compare the electrocatalytic activity, the currents normalized by the mass loading of Pt are shown in Fig. 8b. The peak current densities of Pt$_4$Cu-SMPBs and -M are 0.66 mA µg^{-1} and 1.12 mA µg^{-1}, respectively, which are 1.14-times and 1.93-times higher than that of Pt/C (0.58 mA µg^{-1}). Potential-dependent steady-state currents were measured for the durability test.[1,4] The results in Fig. S11† reveal that the Pt$_4$Cu-SMPBs and -M have better performance for the MOR than the Pt/C for all applied potentials.

4.   Conclusions

The present work has demonstrated a new, cost-effective ORR catalyst through oriented attachment growth based on Pt$_4$Cu sub-nanometer truncated octahedral nanoparticles as building blocks to attach to Pt$_4$Cu-SMPB/-M. The surface energy and surface-to-volume ratio might play the major role in the formation process to minimize the total surface energy under the interaction system. The generated MF structures have 3D surface molecular accessibility with the optimal use of Pt. The Pt$_4$Cu-SMPB/-M exhibited substantial enhancement in both activity and durability towards the ORR and MOR benchmarked against the commercial Pt/C. The results indicate that it is possible to achieve higher catalytic activity with less Pt by using well-defined and controllable particles as building blocks. This oriented attachment growth approach presented here for the structural evolution of bimetallic nanostructures from sub-nanometer single nanoparticles to highly open MF nanostructures can be readily applied to other multimetallic electrocatalysts.

Acknowledgements

Notes and references

1 M. K. Debe, *Nature*, 2012, **486**, 43–51.
2 X. Wang, S. Choi, L. T. Roling, M. Luo, C. Ma, L. Zhang, M. Chi, J. Liu, Z. Xie, A. Jeffrey, M. HerronMavrikakis and Y. N. Xia, *Nat. Commun.*, 2015, **6**, 7594.

3 P. Strasser, S. Koh, T. Anniyev, J. Greeley, K. More, C. Yu, Z. Liu, S. Kaya, D. Nordlund, H. Ogasawara, M. F. Toney and A. Nilsson, *Nat. Chem.*, 2010, **2**, 454–460.

4 K. Sasaki, H. Naohara, Y. Choi, Y. Cai, W. Chen, P. Liu and R. R. Adzic, *Nat. Commun.*, 2012, **3**, 1115.

5 J. Greeley, I. E. L. Stephens, A. S. Bondarenko, T. P. Johansson, H. A. Hansen, T. F. Jaramillo, J. Rossmeisl, I. Chorkendorff and J. K. Nørskov, *Nat. Chem.*, 2009, **1**, 552–556.

6 J. Wu, J. Zhang, Z. Peng, S. Yang, F. T. Wagner and H. Yang, *J. Am. Chem. Soc.*, 2010, **132**, 4985.

7 J. Greeley and M. Mavrikakis, *J. Am. Chem. Soc.*, 2004, **126**, 3910–3919.

8 I. E. L. Stephens, A. S. Bondarenko, F. J. Perez-Alonso, F. Calle-Vallejo, L. Bech, T. P. Johansson, A. K. Jepsen, R. Frydendal, B. P. Knudsen, J. Rossmeis and I. Chorkendorff, *J. Am. Chem. Soc.*, 2011, **133**, 5485–5491.

9 Y. Zuo, K. Cai, L. Wu, T. Li, Z. Lv, J. Liu, K. Shao and H. Han, *J. Mater. Chem. A*, 2015, **3**, 1388–1391.

10 X. Q. Huang, Z. P. Zhao, L. Cao, Y. Chen, E. Zhu, Z. Lin, M. Li, A. Yan, A. Zettl, Y. Wang, X. Duan, T. Mueller and Y. Huang, *Science*, 2015, **348**, 1230–1234.

11 B. Lim, M. Jiang, P. H. C. Camargo, E. C. Cho, J. Tao, X. Lu, Y. Zhu and Y. N. Xia, *Science*, 2009, **324**, 1302–1305.

12 C. Chen, Y. J. Kang, P. D. Yang, V. R. Stamenkovic, *et al.*, *Science*, 2014, **303**, 1339–1343.

13 Y. Wang, S. Choi, X. Zhao, S. Xie, H.-C. Peng, M. Chi, C. Huang and Y. N. Xia, *Adv. Funct. Mater.*, 2014, **24**, 131.

14 A. Tao, S. Habas and P. D. Yang, *Small*, 2008, **4**, 310.

15 Y. N. Xia, Y. Xiong, B. Lim and S. E. Skrabalak, *Angew. Chem., Int. Ed.*, 2009, **48**, 60–103.

16 R. L. Penn and J. F. Banfield, *Science*, 1998, **281**, 969.

17 S. Papadimitriou, S. Armyanov, E. Valova, A. Hubin, O. Steenhaut, E. Pavlidou, G. Kokkinidis and S. Sotiropoulos, *J. Phys. Chem. C*, 2010, **114**, 5217–5223.

18 J. Tang, L. Deng, S. Xiao, H. Deng, X. Zhang and W. Hu, *J. Phys. Chem. C*, 2015, **119**, 21515–21527.

19 H. Zhang, M. Jin, Y. Xiong, B. Lim and Y. N. Xia, *Acc. Chem. Res.*, 2013, **46**, 1783–1794.

20 M. Escudero-Escribano, P. Malacrida, M. H. Hansen, U. G. Vej-Hansen, A. Velázquez- Palenzuela, V. Tripkovic, J. Schiøtz, J. Rossmeisl, I. E. L. Stephens and I. Chorkendorff, *Science*, 2016, **352**, 73–76.

21 B. Zhang, Z. Zhang, H. Liao, Y. Gong, L. Gu, X. Qu, L. You, S. Liu, L. Huang, X. Tian, R. Huang, F. Zhu, T. Liu, Y. Jiang, Z. Zhou and S. G. Sun, *Nano Energy*, 2015, **19**, 198–208.

22 Y. Shao-Horn, W. C. Sheng, S. Chen, P. J. Ferreira, E. F. Holby and D. Morgan, *Top. Catal.*, 2007, **46**, 285.

23 J. Kibsgaard, A. Jackson and T. F. Jaramillo, *Nano Energy*, 2016, DOI: 10.1016/j.nanoen.2016.05.005.

24 H. Kim, S. Cho, Y. Sa, S.-M. Hwang, G.-G. Park, T. Shin, H. Jeong, S.-D. Yim and S. Joo, *Small*, 2016, DOI: 10.1002/smll.201601825.

25 S. Henninga, L. Kühnb, J. Herranza, J. Dursta, T. Binningera, M. Nachtegaalc, M. Werheidb, W. Liub, M. Adamd,

S. Kaskeld, A. Eychmüllerb and T.-J. Schmidt, *J. Electrochem. Soc.*, 2016, **163**, F998–F1003.

26 L. Zhang, L. T. Roling, X. Wang, M. Vara, M. Chi, J. Liu, S. Choi, J. Park, J. A. Herron, Z. Xie, M. Mavrikakis and Y. N. Xia, *Science*, 2015, **349**, 412–416.

27 G. Wang, B. Huang, L. Xiao, Z. Ren, H. Chen, D. Wang, H. D. Abruña, J. Lu and L. Zhuang, *J. Am. Chem. Soc.*, 2014, **136**, 9643.

28 H. Mistry, A. S. Varela, S. Kühl, P. Strasser and B. R. Cuenya, *Nature Reviews Materials*, 2016, **1**, 1–14.

29 C. Zhu, D. Du, A. Eychmuller and Y. Lin, *Chem. Rev.*, 2015, **115**, 8896–8943.

30 B. Xia, N. W. Theng, H. Wu, X. Wang and X. W. (David) Lou, *Angew. Chem., Int. Ed.*, 2012, **51**, 7213–7216.

31 B. Y. Xia, H. B. Wu, X. Wang and X. W. Lou, *J. Am. Chem. Soc.*, 2012, **134**, 13934–13937.

32 A. Oh, H. Baik, D. S. Choi, J. Y. Cheon, B. Kim, H. Kim, S. J. Kwon, S. H. Joo, Y. Jung and K. Lee, *ACS Nano*, 2015, **9**, 2856.

33 R. M. Arán-Ais, J. M. Feliu and P. Strasser, *Nano Lett.*, 2015, **15**, 7473–7480.

34 L. Gan, C. Cui, M. Heggen, F. Dionigi, S. Rudi and P. Strasser, *Science*, 2014, **346**, 1502–1506.

35 V. R. Stamenkovic, B. Fowler, B. S. Mun, G. Wang, P. N. Ross, C. A. Lucas and N. M. Markovic, *Science*, 2007, **315**, 493–497.

36 F. Tao, M. E. Grass, Y. Zhang, D. R. Butcher, J. R. Renzas, Z. Liu, J. Y. Chung, B. S. Mun, M. Salmeron and G. A. Somorjai, *Science*, 2008, **322**, 932–934.

37 M. K. Carpenter, T. E. Moylan, R. S. Kukreja, M. H. Atwan and M. M. Tessema, *J. Am. Chem. Soc.*, 2014, **134**, 8535–8542.

38 Y. Shiraishi, H. Sakamoto, Y. Sugano, S. Ichikawa and T. Hirai, *ACS Nano*, 2013, **7**, 9287–9297.

39 M. Wang, W. Zhang, J. Wang, A. Minett, V. Lo, H. Liu and J. Chen, *J. Mater. Chem. A*, 2013, **1**, 2391–2394.

40 Y. N. Xia, X. Xia and H. Peng, *J. Am. Chem. Soc.*, 2015, **137**, 7947–7966.

41 Y. Zuo, L. Wu, K. Cai, T. Li, W. Yin, D. Li, N. Li, J. Liu and H. Han, *ACS Appl. Mater. Interfaces*, 2015, **7**, 17725–17730.

42 H. Zhang, M. S. Jin and Y. N. Xia, *Angew. Chem., Int. Ed.*, 2012, **51**, 7656–7673.

43 W. Yu, M. D. Porosoff and J. G. Chen, *Chem. Rev.*, 2012, **112**, 5780.

44 F. Saleem, Z. Zhang, B. Xu, X. Xu, P. He and X. Wang, *J. Am. Chem. Soc.*, 2013, **135**, 18304–18307.

45 X. H. Sun, K. Z. Jiang, N. Zhang, S. J. Guo and X. Q. Huang, *ACS Nano*, 2015, **9**, 7634–7640.

46 Y. Zhou and D. M. Zhang, *J. Power Sources*, 2015, **278**, 396–403.

47 Y. Y. Jia, Y. Q. Jiang and Z. X. Xie, *J. Am. Chem. Soc.*, 2014, **136**, 3748–3751.

48 J. Ding, X. Zhu, L. Bu, J. Yao, J. Guo, S. Guo and X. Huang, *Chem. Commun.*, 2015, **51**, 9722–9725.

49 Y. J. Feng, T. He and N. Alonso-Vante, *Fuel Cells*, 2010, **1**, 77–83.

50 Z. Ma, X. Xie, X. Ma, D. Zhang, Q. Ren, N. Heß-Mohr and V. M. Schmidt, *Electrochem. Commun.*, 2006, **8**, 389–394.